The Electrochemical Society
Advancing solid state & electrochemical science & technology

A Polymer-Rich Quaternary Composite Solid Electrolyte for Lithium Batteries

View the article online for updates and enhancements.

A Polymer-Rich Quaternary Composite Solid Electrolyte for Lithium Batteries

Hilal Al-Salih,[1] **Allan Huang,**[2] **Chae-Ho Yim,**[2] **Annica I. Freytag,**[3] **Gillian R. Goward,**[3] **Elena Baranova,**[1] **and Yaser Abu-Lebdeh**[2,z]

[1]*Department of Chemical and Biological Engineering, Centre for Catalysis Research and Innovation, University of Ottawa, Ottawa, Ontario K1N 6N5, Canada*
[2]*Energy, Mining, and Environment Research Centre, National Research Council of Canada, Ottawa, Ontario K1A 0R6, Canada*
[3]*Department of Chemistry and Chemical Biology, McMaster University, Hamilton, Ontario L8S 4M1, Canada*

All-solid-state batteries continue to grow as an alternative to replace the traditional liquid-based ones not only because they provide increased safety but also higher power and energy densities. However, current solid-state electrolytes are either ceramics that are brittle but highly conducting (e.g. $Li_{0.33}La_{0.55}TiO_3$, LLTO) or polymer electrolytes that are poorly conducting but form flexible films with desired mechanical properties (e.g. Poly(ethylene oxide):Lithium bis(trifluoromethanesulfonyl)imide, PEO:LiTFSI). In this work, we have developed quaternary composite solid-state electrolytes (CSEs) to combine the benefits of the two types along with Succinonitrile (SN) as a solid plasticizer. CSEs with different compositions have been fully characterized over the whole compositional range. Guided by neural network simulation results it has been found that a polymer-rich CSE film gives the optimal ionic conductivity ($>10^{-3}$ S cm^{-1} at 55 °C) and mechanical properties (Tensile strength of 16.1 MPa; Elongation-at-break of 2360%). Our solid-state coin-type cell which employs our in-house made cathode shows good cycling performance at C/20 and 55 °C maintaining specific discharge capacity at 143.2 mAh g^{-1} after 30 cycles. This new approach of formulating quaternary CSEs is proven to give the best combination of properties and should be universal and be applied to other CSEs with different chemistry.
© 2020 The Author(s). Published on behalf of The Electrochemical Society by IOP Publishing Limited. This is an open access article distributed under the terms of the Creative Commons Attribution 4.0 License (CC BY, http://creativecommons.org/licenses/by/4.0/), which permits unrestricted reuse of the work in any medium, provided the original work is properly cited. [DOI: 10.1149/1945-7111/ab7fb8]

High energy density, high output voltage and long cycle life with low capacity fading are the attractive characteristics that drove the world towards researching and utilizing lithium ion batteries.[1–4] Nowadays, they are the most commercially used batteries and are the leading power sources for electric vehicles (EV's) and other energy storage applications.[3,4] However, there are some safety hazards accompanying most commercial batteries and this is mainly attributed to the fact that they utilize organic liquid electrolytes which serves as a medium for dendrite formation and always possess the risks of leakage, volatilization, thermal instability and internal short circuiting. The radical solution to eliminate all the above mentioned risks has been found to be the utilization of solid-state electrolytes to form all solid-state batteries.[5–7] In addition to being safer, polymer-based solid-state electrolytes are flexible, mechanically strong and they offer higher power and energy densities as well as better thermal and electrochemical stabilities.[8,9] Noteworthy, being flexible allows their incorporation in various flexible electronics such as implantable biomedical devices, wearable electronics and sensors.[10] For the past decade, researchers have been proposing different strategies to create flexible battery components.[11–15] Although the use of liquid electrolytes in flexible batteries is possible, it is highly recommended to avoid their use because of the above mentioned disadvantages.

One approach to calm the safety hazards associated with liquid electrolytes, is confining them in a solid polymer matrix. This gives the electrolyte mechanical strength yet, the ionic conductivity remains a function of the specific liquid electrolyte and its amount. This type of electrolyte is termed "gel polymer electrolyte" or "gel electrolyte."[16–19] Unfortunately, the performance of gel electrolytes depends on the amount of liquid electrolyte in them and thus, they possess the same risk as the conventional liquid electrolyte especially under demanding operational conditions.[20] Consequently, researchers turned their attention towards the development of completely dry solid electrolytes to ensure total safety. Ionic

conduction mechanism is the same in both solid and liquid lithium-ion batteries. In both, the lithium-ions de-intercalate from the cathodic side and get transported through the electrode-electrolyte interface and the electrolyte until they reach the anode. The only difference between the two batteries is that there is no need for a separator in the solid-state battery because the electrolyte itself acts as one.[21] Solid-state electrolytes are mainly divided into two main classes, the inorganic solid electrolytes (ISE) and the solid polymer electrolytes (SPE). Different classes of ISE have been intensively researched. Although ISE have a generally lower ionic conductivity than liquid electrolytes, researchers have been able to explore a variety of ISE with conductivities that are comparable and even higher than liquid electrolytes.[22–24] Perovskite ISE possess high oxidation potential and mechanical strength but, are unstable when in contact with lithium[25,26] and suffer from high grain boundary resistance.[27] Likewise, NASICON-like ISE show high oxidation potential, high ionic conductivity but are brittle and unstable against lithium metal.[28,29] On the other hand, garnet ISEs (e.g. LLZO) are stable with lithium metal but are hygroscopic and reactive with moisture.[30,31] Similarly, sulfides suffer from sensitivity towards moisture despite having impeccable ionic conductivity.[8,32] Further, high electrode/electrolyte interfacial resistance is observed when applying any kind of ISE, which is attributed to their crystalline structure. This, alongside their large-scale manufacturing difficulties impedes their large scale application.[28]

On the other hand, numerous SPEs based on high molecular weight polymers have been studied. All SPEs share the advantage of flexibility, ease of processability and relatively better electrode/electrolyte interfacial compatibility when compared to ISE.[33] In particular, the polymer polyethylene oxide (PEO) has been found suitable for all-solid-state battery applications. It is applied in the form of a free standing film without major change in the current design of batteries.[34] Also, PEO is known for its ability to solvate various lithium salts by the interaction of ether oxygens with lithium cations.[35,36] Nevertheless, its application is heavily hindered by the low room temperature conductivity ($10^{-6}-10^{-8}$ S cm^{-1}) which is partly because of the high degree of crystallinity of PEO below its

[z]E-mail: Yaser.Abu-Lebdeh@nrc-cnrc.gc.ca

melting point (∼60 °C).[37,38] To develop SPEs with good ionic conductivity and mechanical properties, researchers investigated methods to reduce PEO crystallinity at low temperatures. Possible methods include the addition of inorganic ceramic fillers (ex. Al_2O_3, SiO_2)[39,40] or organic plasticizers (SN, PEG).[41–43] Those fillers are passive fillers as they provide no direct contribution to Li-ion conductivity. Differently, there are fillers termed "active fillers" as they provide alternative pathways for Li-ion migration and thus directly contribute to a substantial increase in ionic conductivity.[44,45] Examples of active fillers are ISEs themselves when added in small amounts to SPEs creating what can be termed as composite solid electrolyte (CSE) or sometimes termed hybrid solid electrolyte (HSE). In the past decade, research has been directed towards different hybrid and CSE materials with a focus on exploring different fillers with SPEs and ISEs. In general, CSEs can be classified into two types based on the relative amounts of ceramic and polymer in the CSE: (1) Polymer-rich or ceramic-in-polymer CSEs where the polymer is the primary phase and its amount is greater than that of the secondary phase ceramic (2) Ceramic-rich or polymer-in-ceramic where the ceramic is the primary phase and its amount in the composite is greater than that of the secondary phase polymer. The properties of the CSE is then governed by those of the primary phase hence each type has its own pros and cons. For example, the polymer-rich CSE has the advantage of retaining the polymer's properties of ease of processability and flexibility and good contact with the electrodes while the ceramic-rich CSE retains the high ionic conductivity and non-flammability of the ceramic.

Most of the studies in the literature are focused on ternary CSEs comprised of a polymer, a ceramic and one of the fillers and seldom on quaternary CSEs. Therefore, in this work we report on a novel type of polymer-rich CSE where both active and passive fillers are used to produce a novel quaternary CSEs with enriched properties. The active filler used is the ISE fast-ionic conductor $Li_{0.34}La_{0.51}TiO_3$ (LLTO) perovskite ceramic and the passive filler is the organic plasticizer "Succinonitrile" (SN), as depicted in the schematic in Fig. 1a. An investigation was executed to find out the appropriate compositions of PEO/LiTFSI/LLTO/SN (quaternary electrolytes) that would provide a highly conductive, free-standing CSE film as shown in Fig. 1b. Then, a full chemical, thermal, mechanical and electrochemical characterization of a selected composition was carried out and battery performance was evaluated in solid-state batteries.

Experimental

Materials.—LLTO (NANOMYTE) was purchased from NEI corporation, PEO (average Mw = 600,000 g mol^{-1}), LiTFSI salt and Acetonitrile were purchased from Sigma-Aldrich and Succinonitrile (SN) was purchased from Fluka. $Li(Ni_{0.5}Mn_{0.3}Co_{0.2})O_2$ (NMC532) was purchased from MTI Corp.

Preparation of CSE films.—LiTFSI and LLTO powders were vacuum dried for 24 h at 80 °C while PEO and SN were dried under vacuum at 40 °C to prevent their melting. The thin CSE films were prepared using the traditional solution casting method. In a small vial, PEO powder was first dispersed in methanol in order to prevent agglomeration and then the main solvent acetonitrile was added to the vial to amount the PEO concentration to 7.3%. The PEO was then allowed to fully dissolve in acetonitrile using mechanical stirring for 2 h. LLTO and SN were then added to the solution and mechanically stirred for 24 h. Then, LiTFSI salt, in the 40:1 EO:Li ratio, was added and the solution continued to stir for another 4 h before it was casted on circular mirror plates. The film was then air dried for 12 h in a convection oven while covered with an acetonitrile wetted cloth to slow down evaporation in order to achieve homogenously looking films, as shown in Fig. 1c. Films were then dried under vacuum for 24 h to completely release any trapped solvent.

Sample characterization.—The mechanical strength of the fully dried films was quantitatively measured by examining the stress-strain relationship using MTS Insight Electro-mechanical load
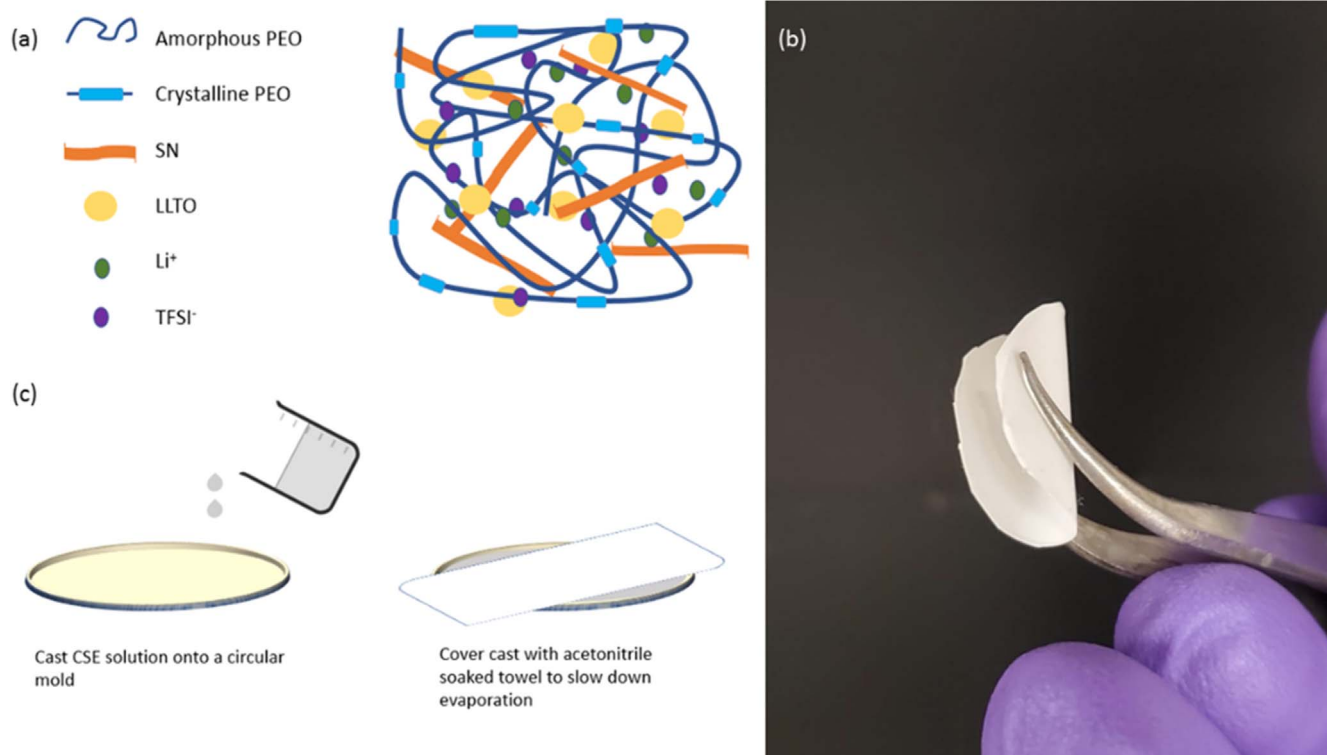

Figure 1. (a) A schematic of the CSE film depicting all its components. (b) CSE film. (c) A schematic of the casting process used to produce the homogenous CSE films depicted in (b).

frame. The films were cut into rectangular coupons that were 15 mm long and 100 mm wide. The test was carried out with a tensile speed of 1 mm min^{-1}.

X-ray diffraction (XRD) measurements were conducted in the Bruker D8 phaser diffractometer with Cu Kx radiation ($\lambda = 1.545$) from $2\theta = 10° - 80°$ with a step of magnitude 5° per min. Further, Thermo-gravimetric analysis (TGA) was performed with Q5000 iR TA instrument. The CSE samples were heated in a sample pan from 25 °C to 600 °C. The heating was done in platinum pans under a N$_2$ purge gas flow of 25 cc min^{-1} at a rate of 10 °C min^{-1}. Differential Scanning Calorimetric (DSC) analysis was performed using Q2000 TA instrument. All the samples were sealed in aluminum hermetic pans and scanned from −90 °C to 100 °C at 10 °C min^{-1} rate under a N$_2$ purge gas flow of 50 cc min^{-1}.

Infrared spectra were recorded using Thermo Fisher Nicolet 6700 with a KBr beam splitter from 4000 to 500 cm^{-1} at 4 cm^{-1} resolution and 32 scans at room temperature. Attenuated Total Reflection (ATR) single bounce with diamond crystal was used as an accessory.

The ionic conductivity of the CSE film was calculated by running Electrochemical Impedance Spectroscopy (EIS) in the frequency range of 10^6 Hz to 1 Hz with an amplitude of 10−50 mV using solatron 1287 frequency analyzer. The CSE thin films were sandwiched between 2 symmetrical blocking stainless steel electrodes of diameter 22.8 mm and their ionic conductivity was determined as a function of temperature between 30 °C and 70 °C with one hour rest time between measurements. The ionic conductivity was calculated using the following equation:

$$\sigma = \frac{L}{AR} \quad [1]$$

Where σ (S/cm) is the ionic conductivity, L (cm) is the film thickness R (Ω) is the bulk resistance and A (cm^2) is the area of the symmetrical electrode. The activation energy was calculated from the Arrhenius plot using the Arrhenius equation:

$$\sigma = \sigma\text{o} \exp\left(\frac{-Ea}{RT}\right) \quad [2]$$

Where σ (S/cm) is the ionic conductivity, σ_o is the pre-exponential factor, E$_a$ is the activation energy, R is the universal gas constant and T is temperature.

All NMR measurements were performed on a 300 MHz spectrometer fitted with a variable temperature unit using a Diff50 probe. For ^{7}Li NMR measurements the CSE film was cut into a rectangular sheet and rolled up to fit inside a 4 mm magic angle spinning rotor. The rotor was then inserted into a 5 mm NMR tube. This allows for easy cleaning of the NMR tube and even distribution of the sample inside the spectrometer. The film was then heated at 75 °C for 4 h inside the magnet before conducting diffusion measurements. Measurements were performed between 30 °C–70 °C. A 20-minute waiting period was included before running diffusion measurements to allow for the sample to equilibrate at the correct temperature (range: 30 °C–70 °C). A stimulated echo gradient pulse sequence was used with the gradient length δ fixed at 2.5 ms and the diffusion time Δ set between 30–200 ms. The b values were kept constant for each temperature by varying the applied gradient strength and the diffusion time. The number of scans varied between 32 and 1024 scans with the gradient steps being kept constant at 32. Recycle delays were set between 1.0–2.5 s. T2 relaxation of LLTO is approximately an order of magnitude smaller than in LiTFSI, leading to a filtering of the LLTO signal under the above conditions. Solely the dynamics of LiTFSI in the polymer matrix is observed in this study. Diffusion data sets were fit using a single or (where applicable) multi-component fit in Matlab.

The electrochemical stability window was determined by linear sweep voltammetry (LSV) experiments which were run in a two-electrode cell fitted with stainless steel electrodes using Biologic

VMP3 potentiostat. The scanning rate chosen was 50 mVs^{-1} at 55 °C from −4 V to 4 V.

Battery assembly and testing.—To test the battery performance of these solid-state electrolytes, an all-solid-state 2325 coin-type half cells were assembled. Lithium metal discs were used as the counter electrode and an in-house made cathode was prepared to incorporate the PEO:LiTFSI electrolyte. The cathode composition (wt%) is as follows: 70% NMC 532, 15% PEO:LiTFSI (2:1), 10% Carbon C65 and 5% PVDF. The cathode slurry was prepared by adding pre-dissolved 2.5 wt% PVDF in NMP to 11.5 wt% PEO/LiTFSI in acetonitrile. C65 and NMC 532 are then added sequentially. The cathode was then cast on aluminum current collector and then dried at 80 °C for 24 h. The cathode was then calendared and was ready for use. 0.5″ diameter circular cuts were taken for coin-type cell assembly in an Argon filled glove box by sandwiching a 0.7″ solid electrolyte cut in between a 0.7″ Li disc and the cathode cut. The fabricated cells were then heated to 70 °C for 4 h, then cooled down and capacity measurements were performed by galvanostatic experiments carried out on a multichannel Arbin battery cycler (BT2000). This heating cycle is essential to homogenise the sample and stabilize the electrode/electrolyte interface. Charge-discharge tests were then carried out in the potential range of 2.5–4.2 V at 55 °C.

Results and Discussion

The first step in the preparation of the polymer-rich quaternary CSEs is to select the PEO:LiTFSI (better known as EO:Li) molar ratio. This is better done by the aid of the PEO:LiTFSI phase diagram which is well documented and it shows the formation of three complex compounds at 2:1, 3:1 and 6:1 molar ratios with a crystallinity gap in the eutectic composition region between 12:1 and 6:1.[46] The conductivity isotherms (σ vs T) are also known and similar to most liquid and solid electrolytes; it shows an increase in conductivity with salt addition but goes through a maximum near the eutectic composition and then drops thereafter till the saturation concentration. At room temperature, the conductivity increases from 10^{-8} S cm^{-1} at 48:1 EO:Li to reach a maximum of 10^{-5} S cm^{-1} at 10:1 EO:Li and decreases to 10^{-7} S cm^{-1} at 6:1 EO:Li. while at temperatures around the melting point of pure PEO, a similar trend is observed for the isotherm with an overall increase of one order of magnitude in conductivity values with a maximum still at 10:1. The eutectic composition seems to be a natural choice due to the maximum conductivity, but the mechanical properties are poor due to the crystallinity gap which prevents the formation of free-standing films. In this work, we selected an EO:Li ratio in the polymer-rich side of the phase diagram close to 40:1 where at room temperature pure, solid PEO coexists in equilibrium with either the liquid or (amorphous) solid 6:1 complex. Binary and ternary phase diagrams of PEO, LiTFSI and SN have also been studied and eutectic-type phase diagrams are observed in the binary phases and coexistence regions in the ternary phase diagram have been identified at the end members with a wide isotropic liquid-like regions in the center indicative of the formation of ternary eutectics.[46]

Next, even though we decided to focus on polymer-rich CSE composites which means small amounts of LLTO and SN to act as fillers, CSEs were fabricated in different ratios, to cover the whole compositional range. This includes CSEs with large amounts of LLTO and SN to map out and have an understanding of the structure/property relationship in these previously unknown quaternary CSEs. Then, the obtained properties (mechanical properties and ionic conductivity) were used as data points for non-linear fitting by using a neural network algorithm as described by Li et al.[47] The parameters obtained were used for simulating ternary diagrams. The simulation results were presented as two contour maps for each property, where orange and darker colors indicate free standing films and $\geqslant 10^{-3}$ S cm^{-1} conductivity and blue color indicates no film formation and $\leqslant 10^{-5}$ S cm^{-1} conductivity, respectively. As can be seen in Figs. 2a and 2b, the ternary compositions that are best at film
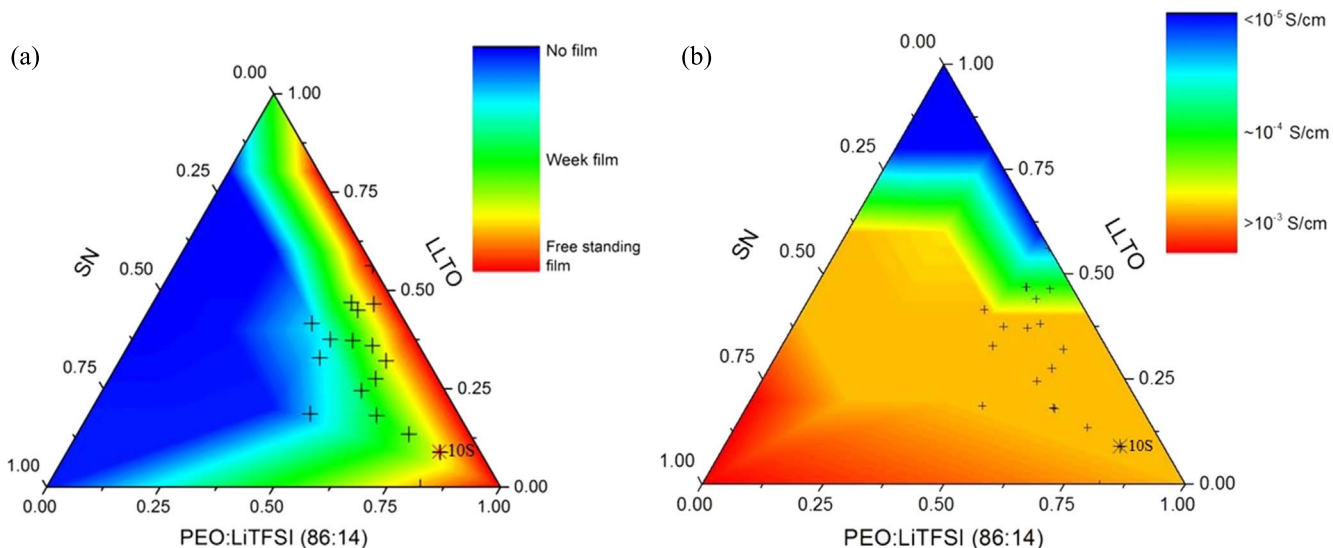
Figure 2. (a) Contour map indicating possible film forming quaternary compositions. PEO/LiTFSI ratio was fixed at 40:1. Orange and darker colors indicate compositions that made free standing films, blue means no film was formed and green indicates weak self-sticking films were formed. (b) similar map indicating the ionic conductivities of the compositions at 55 °C. Orange and darker colors indicate conductivities $>10^{-3}$ S cm^{-1}, blue indicates conductivities $<10^{-5}$ S cm^{-1}.

forming, are mainly concentrated in the polymer-rich or ceramic-in-polymer region, while the conductivity contour map indicates that the SN-rich region shows the highest ionic conductivity. This is expected as SN is known to act as a polymer plasticizer[42] and its high polarity allow for the ease of dissolution of lithium salts.[45] Based on this, the conclusion is that a quaternary composition in the polymer-rich region with small amounts of SN has the optimal combination of electrochemical and mechanical properties. Similar conclusions were drawn by Chen et al. in a study that showed that the role of another ceramic LLZO in similar ceramic-in-polymer composites, but with no SN, is to enhance mechanical properties of the films. It also show that in polymer-in-ceramic composites the ceramic provides a pathway for Li ions and improves the ability of the otherwise organic polymer to withstand stress from dendrites formed during lithium plating/stripping.[48]

The CSE film chosen for full characterization is sample "10S" which lies in the red/orange regions of the two ternary composition diagrams showing the best combination of conductivity and film forming ability. The composition of 10S is 70 wt% PEO, 12 wt% LiTFSI, 9 wt% LLTO and 9 wt% SN. The morphology and chemical composition of the sample were studied by SEM and EDS and

images in Figs. 3a and 3b indicate that LLTO particles (∼2 μm) and LiTFSI salt are homogeneously dispersed in the porous polymer matrix.

Electrochemical Impedance Spectroscopy (EIS) was used to measure the conductivity of the 10S CSE film and found to be 1.9×10^{-4} S cm^{-1} at room temperature and 2.4×10^{-3} S cm^{-1} at 55 °C. These values are much higher than the reported values by Fan et al. for PEO:LiTFSI:SN composites with 11:1 EO:Li ratio which is close to the eutectic composition and prone to produce liquid-like films.[42] The reported ionic conductivity at 30 °C reached 5×10^{-4} S cm^{-1} for the 50% SN-containing film and ∼5×10^{-5} S cm^{-1} for the 16% SN-containing film. Even though it gives higher conductivity the use of larger amounts of SN introduces competition between SN (dielectric constant, $\varepsilon = 38$) and PEO (dielectric constant, $\varepsilon = 8$) and this might result in blocking of ionic pathways. Figure 4 shows the σ vs T "Arrhenius" plot for this CSE film. The activation energies of the film were calculated using the Arrhenius equation (Eq. 2) and the linear fitting for the data points in the low temperature region and the high temperature region as can be seen in Fig. 4. The activation energies were found to be 38 ± 4 kJ mol^{-1} and 27 ± 1 kJ mol^{-1}, respectively. This drop in activation energy indicates an increase in the ease in
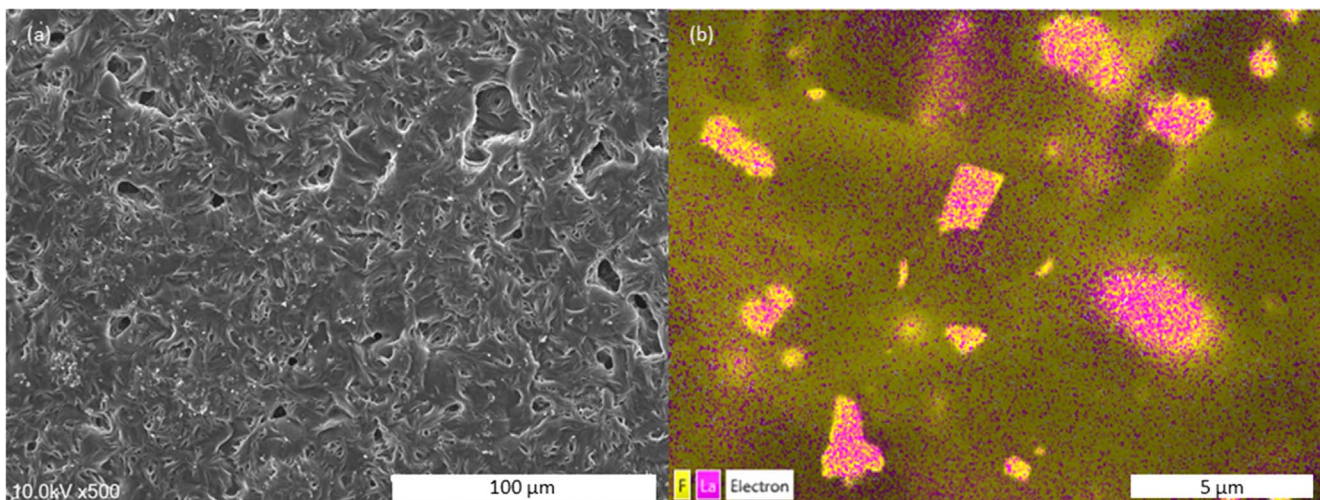

Figure 3. (a) SEM image of the 10S CSE film along with (b) layered EDS image showing the distribution of La (LLTO) and F (LiTFSI) throughout the film.
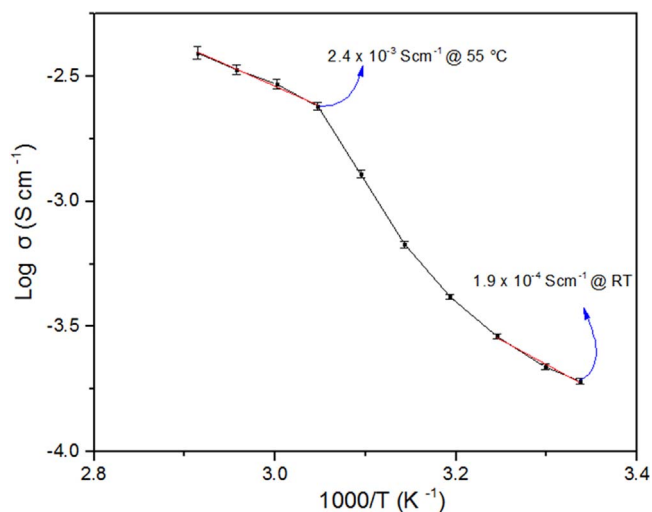
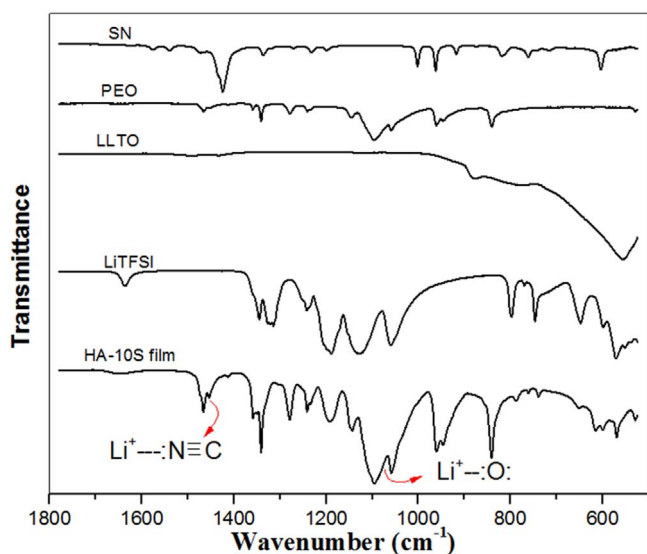**Figure 4.** Conductivity vs T 'Arrhenius plot'' of the 10S CSE film.

Figure 5. ATR FTIR spectra of the 10S CSE film and its components.

which ions move at higher temperatures that is also expected in the molten state. In general, the activation energy values found in this work are similar to those reported by Fan et al.[42] but way lower than those reported by Zhu et al.[44] on PEO:LiTFSI:LLTO nanocomposites. Activation energies higher than 40 kJ mol^{-1} for composites with small amounts of LLTO fiber were reported that are close to those of PEO:LiTFSI ($\sim$50 kJ mol^{-1}).[49] This indicates easier ionic conduction pathways in the quaternary composite compared to ternary composites specially the ones without SN as a plasticizer.

FTIR spectroscopy was utilized to observe and analyze the molecular interactions between the four components in the CSE film and the spectra are shown in Fig. 5. PEO FTIR spectrum contains bands at around 842, 1100 and 1468 cm^{-1} which corresponds to CH$_2$ wagging mode, C–O–C stretching mode and CH$_2$ scissoring mode, respectively.[50] By means of comparison of the FTIR spectra of the 10S CSE film and its individual components, we can notice that the band at around 1470 cm^{-1} splits and becomes sharper which indicates a possible interaction between SN and Li cation of LiTFSI. Besides, we can also observe the broadening of the C–O–C stretching band at around 1100 cm^{-1}. This in turn indicates the coordination of Li$^+$ cation with the ether groups in PEO.[48]

^{7}Li NMR spectroscopy was also performed for the 10S CSE film to get more insight on this interaction and ion dynamics at different temperatures. The spectra shown in Fig. 6a reveal a single, broad peak throughout the heating and cooling cycles which is attributed to the LiTFSI species. The linewidth decreases with increasing temperature indicating a change in ion mobility. Diffusion behavior of PEO-containing polymer electrolytes has been studied extensively in the past.[51] Detailed dynamic NMR studies have revealed the dependence of the cation mobility on the morphology of the polymer matrix.[52,53] It has been shown that an increase in amorphous domains leads to a better-connected conductive networks. In particular, the polymer chain motion is essential in facilitating ionic diffusion in polymer electrolytes.[54,55] ^{7}Li pulsed field gradient (PFG) NMR was performed in order to investigate ionic diffusion in the 10S CSE film. Diffusion curves were obtained in the range of 30 °C–70 °C and are shown in Fig. 6b. At high temperatures a single diffusion process dominates, allowing for an accurate single-component fit while a single-component fit is not appropriate at lower temperatures. It is evident, that there is a significant change in the diffusion behavior between 45 °C to 55 °C. At high temperatures (55 °C to 70 °C) a linear dependence is apparent while at intermediate temperatures a coexistence of two components with slightly different diffusivities is apparent. This is in agreement with the change of morphology around the transition temperature, where presumably regions with varying degree of crystallinity are apparent. This gradual phase change is observed around 50 °C, which shows a deviation from linear behavior in the Arrhenius plot in Fig. 6b. These two different regions have contrasting diffusion behavior with activation energies for region I and region II of 37 ± 1 kJ mol^{-1} and 67 ± 1 kJ mol^{-1}, respectively. However, the change in activation energy with temperature is in line with what was observed earlier in the Arrhenius plots obtained from ionic conductivity measurements and can be attributed to polymer morphology which has a significant influence on the diffusion pathways besides a possible role of SN. This might indicate that in polymer-rich CSE composites the ionic conductivity is dominated by the polymer dynamics and not the ceramic as was shown by Zheng et al.[56] for LLZO:PEO composites where tracking of Li ion pathways at higher ceramic content proved the dominance of ceramic related pathways.

To further understand the effect of SN as a plasticizer, the phase transition behavior of 10S film was compared to that of a film made with the same ratios of 10S CSE film but without the SN, hereafter called "10S-SN." Figure 7 shows the DSC scans which demonstrates a clear glass transition temperature (T$_g$) decrease from −42.8 °C for 10S-SN to −53.1 °C for the 10S CSE film. A reduction in T$_g$ enables faster ionic kinetics in polymer electrolytes.[57] Other features clear on the DSC curves of both samples is the endothermic peak shortly after 50 °C which corresponds to the melting of PEO. The 10S CSE film (SN containing) shows a marginal shift to the left because of the melting point reduction effect due to the presence of SN. Looking closely, the melting peak of 10S-SN is also broader which is attributed to its higher crystallinity. To confirm this, the degree of crystallinity, X$_c$, was calculated using Eq. 3.

$$X_c = \frac{\Delta H_m}{\Delta H_{PEO} \cdot Y_{PEO}} \quad [3]$$

Where ΔH_m is the melting enthalpy of the sample, ΔH_{PEO} is the melting enthalpy of 100% crystalline PEO, 203 J g^{-1}[58,59] and Y_{PEO} is the weight fraction of PEO in the sample. X$_c$ calculations show that 10S-SN is 51.8% crystalline while 10S is 42.6% crystalline. This significant decrease in crystallinity is solely caused by the addition of SN. Similar behavior was observed by Fan et al. for similar compositions but without LLTO, and they showed that higher amounts of SN (50%) result in completely amorphous composites.[42]

PEO is a semi-crystalline polymer where the amorphous phase offers activated and more flexible chain segments which aid ion mobility.[60] Previous reports and studies have attributed PEO's low
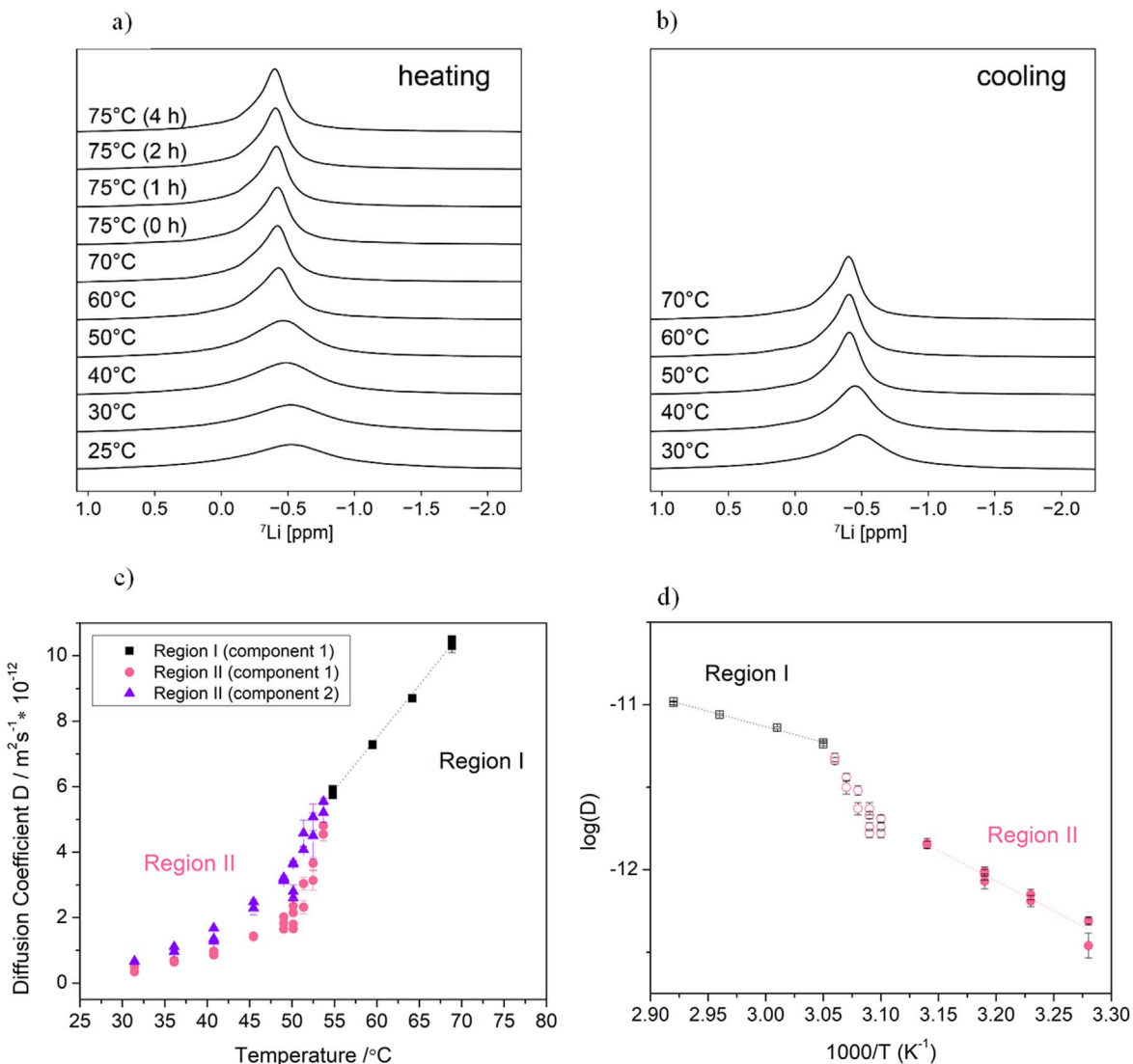
Figure 6. ^{7}Li NMR spectra of the 10S CSE film as a function of temperature during (a) heating cycle, (b) cooling cycle (c) Diffusion coefficients of the 10S CSE film as a function of temperature. (d) Arrhenius plot of the diffusion coefficient.
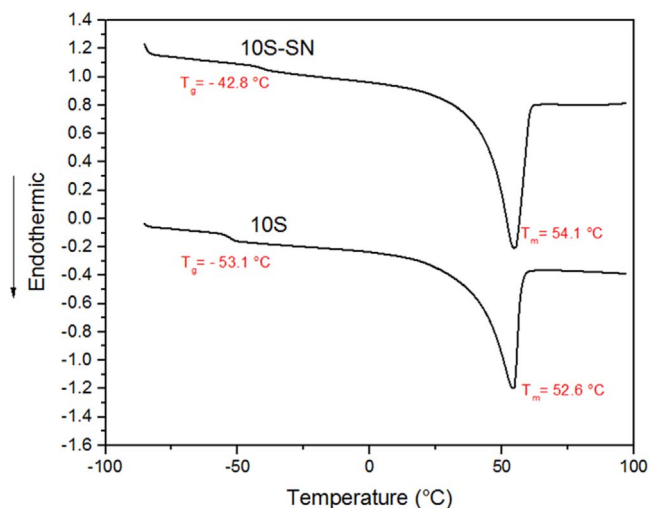

Figure 7. DSC scans of the 10S CSE film with and without succinonitrile (10S-SN).

ionic conductivity to slow polymer chains dynamics and inactive chain segments due to the crystalline phase domination. Hence, studies have been directed towards using fillers that increase the amorphous phase ratio, those are termed "plasticizers." XRD technique was used to investigate the crystal structure of 10S and 10S-SN CSE films. Before the characterization, the two samples underwent a heating cycle by heating to 70 °C for 4 h then cooled back to ambient conditions. Figure 8 shows the clear disappearance of two major peaks related to PEO crystalline phase peaks at around 19° and 23°. This further proves the effectiveness of SN in the CSE as it plays both the role of Li$^+$ solvation and PEO chain plasticization which in turn explains the high ionic conductivity of this electrolyte.

Furthermore, the thermal stability of the 10S CSE film was investigated by means of TGA. Solid-state electrolytes must possess high degrees of thermal stability. This is to ensure safety and justify their use over liquid electrolytes. The TGA profile for 10S shown in Fig. 9 indicates that there is a slight weight loss happening mainly after 100 °C but the 10S CSE film demonstrates good thermal stability till about 360 °C. Notably, the weight percentage remaining after heating to 600 °C is 12.3 wt% which is slightly higher than the ceramic content in the sample. This difference could correspond to
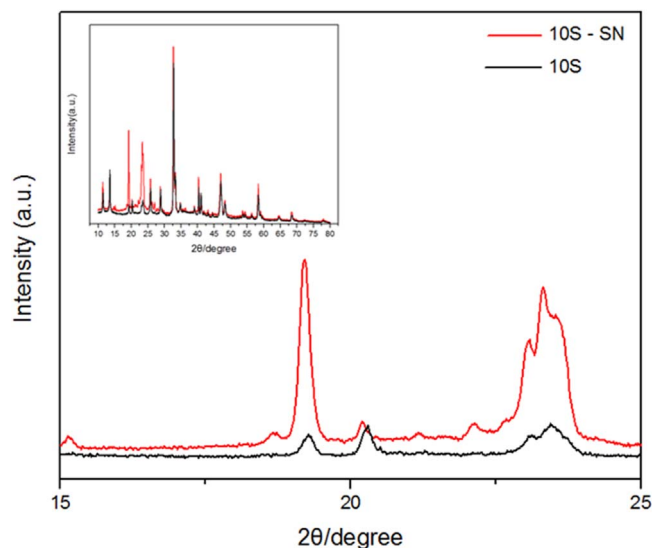
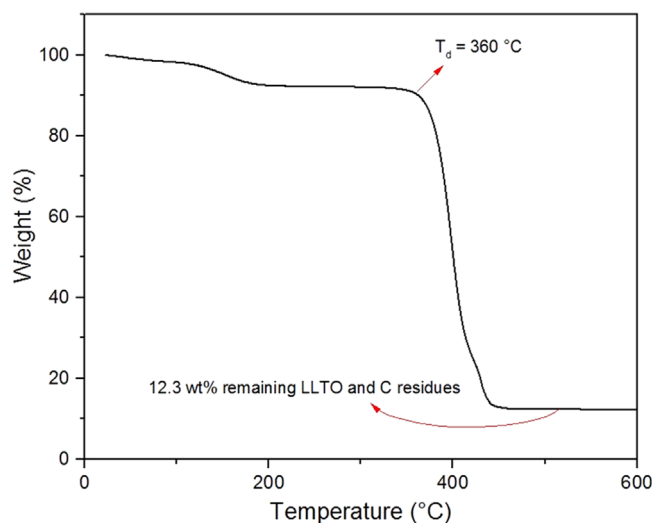**Figure 8.** XRD patterns of the 10S CSE film with and without succinonitrile (10S-SN).

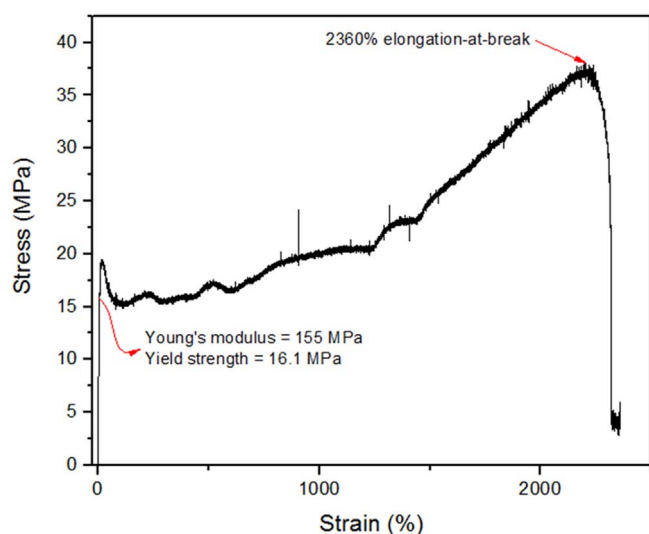**Figure 9.** TGA scan of the 10S CSE film.

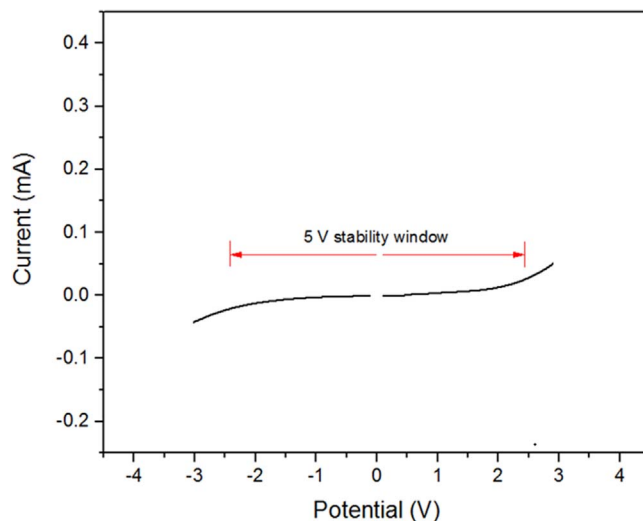**Figure 10.** Stress strain test of the 10S CSE film.

Figure 11. LSV scan of the 10S CSE film.

carbon residues remaining after complete degradation. Echeverri et al.[46] reported the TGA scans of PEO, LiTFSI and SN and showed that while both neat PEO and LiTFSI have high thermal stability up to 380 °C the neat SN is only stable up to 130 °C upon prolonged heating. This can explain the small weight loss above 100 °C in the 10S CSE film.

The mechanical properties of 10S CSE film was measured by stress-strain testing. A good CSE film should be processed to withstand great forces of stress to ensure it does not fail either during cell packaging or when being charged/discharged. The stress-strain curve for the 10S CSE film is presented in Fig. 10. The film exhibits a Young's modulus of ~155 MPa, a Tensile strength of 16.1 MPa and an elongation-at-break of 2360%. Thus, This CSE film possesses plastic behavior and can be applied as a separator and as an ionic conductor. Fan et al. reported on the mechanical properties of similar composites without LLTO and showed that the addition of 50% SN to PEO:LiTFSI (11:1 EO:Li) resulted in a tensile strength of 0.5 MPa and an elongation-at-break of 550%.[42] The values are way smaller than those of the 10S CSE film which could be attributed to the large amount of SN in the films along with the presence of LLTO in the 10S film which seems to improve the mechanical properties of the quaternary CSE.

Electrochemical stability is another key parameter to develop high energy density lithium batteries. By means of linear sweep voltammetry (LSV), we were able to determine the electrochemical stability window of the 10S CSE film at 55 °C as shown in Fig. 11. We can observe that the oxidation/reduction peaks onset at 2.5 V and −2.5 V respectively which translates to an electrochemical stability window of 5 V.

To assess the electrochemical performance of the 10S CSE film, 2325 coin-type cells were assembled by sandwiching the 10S film between commercial NMC 532 cathode (fabricated following common procedures of mixing NMC 532 powder with PVDF binder and a carbon additive) and a lithium disc. Charge-discharge tests were then carried out in the potential range of 2.5–4.2 V at 55 °C and at a cycling rate of C/20. These cells showed poor cycling performance and provided an initial discharge capacity of only 7 mAh g^{-1}. This is mainly attributed to the poor interfacial contact between the cathode and the electrolyte and the internal resistance inside the cell which was calculated to be 2030 ± 10 Ω. To improve the interfacial resistance, we assembled new coin-type cells which employs our in-house made cathode that utilizes PEO:LiTFSI (2:1) as a co-binder to help improve the cathode/electrolyte interfacial contact. Figure 12 shows the charge-discharge curve and the cycling performance of sample 10S. Notably, the specific discharge capacity improved significantly to values closer to the known experimental
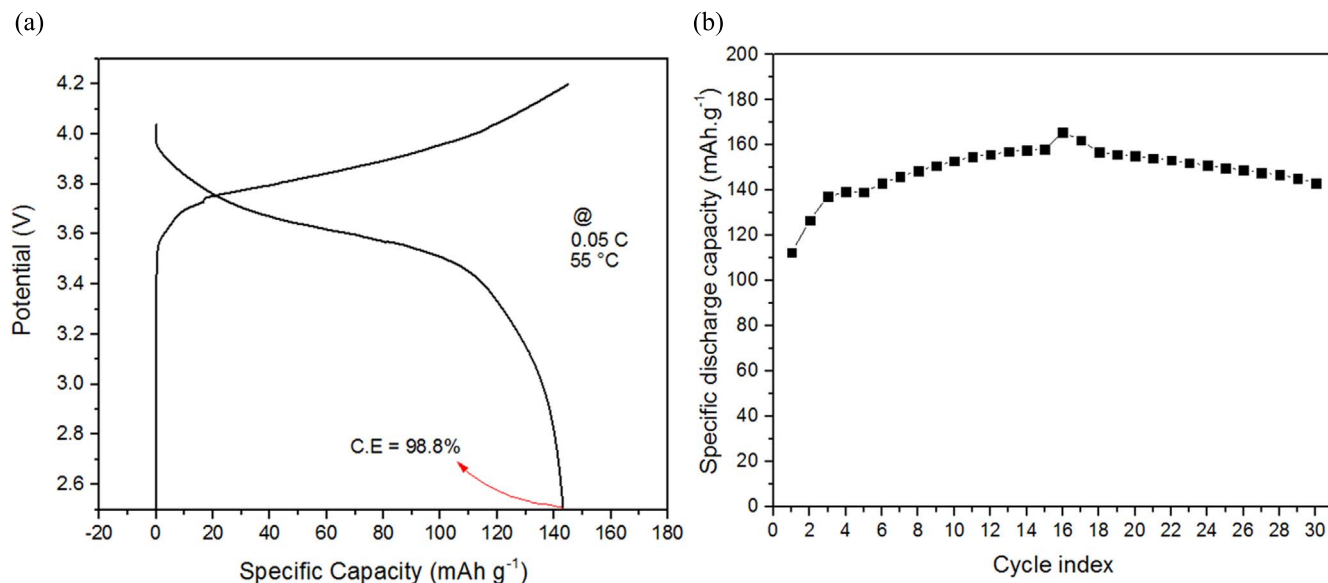
(a)

(b)

Figure 12. (a) Charge-discharge curve of the 10S CSE film at 0.05 C (C/20) and 55 °C (b) Cycling performance at 55 °C.

values ($\sim$150 mAh g^{-1}). The initial capacity reached 112 mA g^{-1} then it kept on increasing for the first 16 cycles which indicates the continuous homogenization of the components inside the composite and at the interface inside the battery. After 30 cycles, the battery discharge capacity reached 143.2 mAh g^{-1} and the columbic efficiency achieved was 98.8%.

Conclusions

A polymer-rich quaternary composite solid-state electrolyte composed of PEO-LiTFSI-LLTO-SN was proposed and well characterized. Simulation done using neural network fitting technique helped us to choose a quaternary sample with an optimal combination of mechanical and electrochemical properties. The chosen CSE film with the following composition: 70 wt% PEO, 12 wt% LiTFSI, 9 wt% LLTO and 9 wt% SN was made using traditional solution casting technique and its ionic conductivity reached slightly higher than 10^{-3} S cm^{-1} at 55 °C. Mechanical testing showed that the film has a Young modulus of $\sim$155 MPa, a Yield strength of around 16 MPa and a break-at-elongation point of over 2000%. FTIR, NMR, DSC and XRD techniques proved with evidence the role of Succinonitrile as a plasticizer, thus, explaining the high ionic conductivity. To fabricate the battery, incorporation of PEO: LiTFSI as a binder in the NMC 532-based cathode was essential to overcome the cathode-electrolyte interfacial resistance issue. The discharge capacity achieved by the battery Li/CSE/NMC 532 after 30 cycles was 143.2 mAh g^{-1} at C/20 and 55 °C. We can conclude that quaternary CSEs are promising candidate for next-generation solid-state lithium batteries.

ORCID

Hilal Al-Salih https://orcid.org/0000-0002-1928-2330
Yaser Abu-Lebdeh https://orcid.org/0000-0001-8936-4238

References

1. M. Armand and J. M. Tarascon, *Nature*, **451**, 652 (2008).
2. J. W. Fergus, *J. Power Sources*, **195**, 939 (2010).
3. C.-Y. Wang, G. Zhang, S. Ge, T. Xu, Y. Ji, X.-G. Yang, and Y. Leng, *Nature*, **529**, 515 (2016).
4. E. Quartarone and P. Mustarelli, "Electrolytes for solid-state lithium rechargeable batteries: Recent advances and perspectives." *Chem. Soc. Rev.*, **40**, 2525 (2011).
5. P. P. Soo, B. Huang, Y. I. I. Jang, Y. M. Chiang, D. R. Sadoway, and A. M. Mayes, *J. Electrochem. Soc.*, **146**, 32 (1999).
6. Y. Zhao, C. Wu, G. Peng, X. Chen, X. Yao, Y. Bai, F. Wu, S. Chen, and X. Xu, *J. Power Sources*, **301**, 47 (2016).
7. Q. Zhao, S. Stalin, C.-Z. Zhao, and L. A. Archer, *Nat. Rev. Mater.*, **5**, 229 (2020).
8. N. Kamaya et al., *Nat. Mater.*, **10**, 682 (2011).
9. K. Xu, "Electrolytes and interphases in Li-ion batteries and beyond." *Chem. Rev.*, **114**, 11503 (2014).
10. H. Nishide and K. Oyaizu, "Toward flexible batteries." *Science (80-.).*, **319**, 737 (2008).
11. A. Goyal, A. L. M. Reddy, and P. M. Ajayan, *Small*, **7**, 1709 (2011).
12. S. Y. Chew, S. H. Ng, J. Wang, P. Novák, F. Krumeich, S. L. Chou, J. Chen, and H. K. Liu, *Carbon N. Y.*, **47**, 2976 (2009).
13. J. Z. Wang, C. Zhong, S. L. Chou, and H. K. Liu, *Electrochem. Commun.*, **12**, 1467 (2010).
14. N. Li, Z. Chen, W. Ren, F. Li, and H. M. Cheng, *Proc. Natl. Acad. Sci. U. S. A*, **109**, 17360 (2012).
15. L. Noerochim, J. Z. Wang, S. L. Chou, D. Wexler, and H. K. Liu, *Carbon N. Y.*, **50**, 1289 (2012).
16. A. M. Stephan, "Review on gel polymer electrolytes for lithium batteries." *Eur. Polym. J.*, **42**, 21 (2006).
17. J. Y. Song, Y. Y. Wang, and C. C. Wan, "Review of gel-type polymer electrolytes for lithium-ion batteries." *J. Power Sources*, **77**, 183 (1999).
18. A. Arya and A. L. Sharma, "Polymer electrolytes for lithium ion batteries: a critical study." *Ionics (Kiel).*, **23**, 497 (2017).
19. I. Osada, H. De Vries, B. Scrosati, and S Passerini, "Ionic-liquid-based polymer electrolytes for battery applications." *Angew. Chemie - Int. Ed.*, **55**, 500 (2016).
20. W. H. Meyer, *Adv. Mater.*, **10**, 439 (1998).
21. F. Zheng, M. Kotobuki, S. Song, M. O. Lai, and L. Lu, *J. Power Sources*, **389**, 198 (2018).
22. Z. Ma, H. G. Xue, and S. P. Guo, "Recent achievements on sulfide-type solid electrolytes: crystal structures and electrochemical performance." *J. Mater. Sci.*, **53**, 3927 (2018).
23. J. C. Bachman et al., "Inorganic solid-state electrolytes for lithium batteries: mechanisms and properties governing ion conduction." *Chem. Rev.*, **116**, 140 (2016).
24. A. Varzi, R. Raccichini, S. Passerini, and B. Scrosati, *J. Mater. Chem. A*, **4**, 17251 (2016).
25. C. H. Chen and K. Amine, *Solid State Ionics*, **144**, 51 (2001).
26. Y. H. Cho, J. Wolfenstine, E. Rangasamy, H. Kim, H. Choe, and J. Sakamoto, *J. Mater. Sci.*, **47**, 5970 (2012).
27. C. Ma, K. Chen, C. Liang, C. W. Nan, R. Ishikawa, K. More, and M. Chi, *Energy Environ. Sci.*, **7**, 1638 (2014).
28. M. Keller, A. Varzi, and S. Passerini, *J. Power Sources*, **392**, 206 (2018).
29. P. Hartmann, T. Leichtweiss, M. R. Busche, M. Schneider, M. Reich, J. Sann, P. Adelhelm, and J. Janek, *J. Phys. Chem. C*, **117**, 21064 (2013).
30. A. Sharafi, E. Kazyak, A. L. Davis, S. Yu, T. Thompson, D. J. Siegel, N. P. Dasgupta, and J. Sakamoto, *Chem. Mater.*, **29**, 7961 (2017).
31. M. Wang and J. Sakamoto, *J. Power Sources*, **377**, 7 (2018).
32. Q. Zhang, D. Cao, Y. Ma, A. Natan, P. Aurora, and H. Zhu, *Adv. Mater.*, **31**, 1901131 (2019).

33. C. Sun, J. Liu, Y. Gong, D. P. Wilkinson, and J. Zhang, "Recent advances in all-solid-state rechargeable lithium batteries." *Nano Energy*, **33**, 363 (2017).
34. B. Scrosati and J. Garche, "Lithium batteries: status, prospects and future." *J. Power Sources*, **195**, 2419 (2010).
35. G. M. St, S. A. Mullin, A. A. Teran, D. T. Hallinan, A. M. Minor, A. Hexemer, and N. P. Balsara, *J. Electrochem. Soc.*, **159** (2012).
36. K. J. Harry, D. T. Hallinan, D. Y. Parkinson, A. A. MacDowell, and N. P. Balsara, *Nat. Mater.*, **13**, 69 (2014).
37. S. K. Fullerton-Shirey and J. K. Maranas, *Macromolecules*, **42**, 2142 (2009).
38. J. G. Kim, B. Son, S. Mukherjee, N. Schuppert, A. Bates, O. Kwon, M. J. Choi, H. Y. Chung, and S. Park, "A review of lithium and non-lithium based solid state batteries." *J. Power Sources*, **282**, 299 (2015).
39. D. Lin, W. Liu, Y. Liu, H. R. Lee, P. C. Hsu, K. Liu, and Y. Cui, *Nano Lett.*, **16**, 459 (2016).
40. G. X. Wang, L. Yang, J. Z. Wang, H. K. Liu, and S. X. Dou, *J. Nanosci. Nanotechnol.*, **5**, 1135 (2005).
41. W. Liu, S. W. Lee, D. Lin, F. Shi, S. Wang, A. D. Sendek, and Y. Cui, *Nat. Energy*, **2**, 17035 (2017).
42. L. Z. Fan, Y. S. Hu, A. J. Bhattacharyya, and J. Maier, *Adv. Funct. Mater.*, **17**, 2800 (2007).
43. Y. Masuda, M. Nakayama, and M. Wakihara, *Solid State Ionics*, **178**, 981 (2007).
44. L. Zhu, P. Zhu, Q. Fang, M. Jing, X. Shen, and L. Yang, *Electrochim. Acta*, **292**, 718 (2018).
45. T. Pareek, S. Dwivedi, S. A. Ahmad, M. Badole, and S. Kumar, *J. Alloys Compd.*, **824**, 153991 (2020).
46. M. Echeverri, N. Kim, and T. Kyu, *Macromolecules*, **45**, 6068 (2012).
47. Z. Li, Z. Cheng, L. Xu, and T. Li, *Anal. Chem.*, **65**, 393 (1993).
48. L. Chen, Y. Li, S. P. Li, L. Z. Fan, C. W. Nan, and J. B. Goodenough, *Nano Energy*, **46**, 176 (2018).
49. P. Zhu et al., *J. Mater. Chem. A*, **6**, 4279 (2018).
50. E. Morales and J. L. Acosta, *J. Appl. Polym. Sci.*, **69**, 2435 (1998).
51. S. Munoz and S. Greenbaum, *Membranes (Basel).*, **8**, 120 (2018).
52. W. Gorecki, M. Jeannin, E. Belorizky, C. Roux, and M. Armand, *J. Phys. Condens. Matter*, **7**, 6823 (1995).
53. C. Berthier, W. Gorecki, M. Minier, M. B. Armand, J. M. Chabagno, and P. Rigaud, *Solid State Ionics*, **11**, 91 (1983).
54. J. P. Donoso, T. J. Bonagamba, H. C. Panepucci, L. N. Oliveira, W. Gorecki, C. Berthier, and M. Armand, *J. Chem. Phys.*, **98**, 10026 (1993).
55. W. Gorecki, C. Roux, M. Clémancey, M. Armand, and E. Belorizky, *ChemPhysChem*, **3**, 620 (2002).
56. J. Zheng, M. Tang, and Y.-Y. Hu, *Angew. Chemie Int. Ed.*, **55**, 12538 (2016).
57. V. S. Kolosnitsyn, G. P. Dukhanin, S. A. Dumler, and I. A. Novakov, "Lithium-conducting polymer electrolytes for chemical power sources." *Russ. J. Appl. Chem.*, **78**, 1 (2005).
58. X. L. Wu, S. Xin, H. H. Seo, J. Kim, Y. G. Guo, and J. S. Lee, *Solid State Ionics*, **186**, 1 (2011).
59. L. Hu, Z. Tang, and Z. Zhang, *J. Power Sources*, **166**, 226 (2007).
60. P. Johansson, *Polymer (Guildf).*, **42**, 4367 (2001).